

On the role of vegetation density on net snow cover radiation at the forest floor

Bijan Seyednasrollah,¹ Mukesh Kumar,¹ and Timothy E. Link²

Received 18 April 2013; revised 12 June 2013; accepted 14 June 2013.

[1] The timing and amount of snowmelt from forested watersheds is influenced by the total radiation reaching the forest floor. In order to understand and predict the impact of natural or anthropogenic changes in vegetation density on snow energetics, it is important to first quantify the relationship between vegetation density and net snow cover radiation. A physically based forest radiation model (FoRM) was developed to quantify net radiation on the forest floor and its dependence on vegetation density in midlatitude coniferous forests. For clear sky conditions, net radiation on the horizontal forest floor frequently exhibits a nonmonotonic decreasing then increasing trend with increasing vegetation density. The relationship turns monotonically increasing when cloudiness is considered. Variations in slope and aspect were also found to influence the behavior of radiation in relation to changing vegetation density. Net radiation increases with increasing slope for southerly aspects and decreases with northerly facing aspects. For clear sky conditions on south facing slopes, the optimal vegetation density at which radiation is minimized increases both with slope and toward more southerly aspects. In contrast, on north facing slopes, the vegetation density where net radiation is minimized decreases with increasing slope angle. When sky cloudiness is considered, for increasing south facing slopes, the relationship becomes relatively complex with the appearance of a local minimum at intermediate vegetation densities. The results have implications for prediction of snowmelt dynamics in complex terrain and development of forest thinning strategies to modulate snowmelt timing in mountainous environments.

Citation: Seyednasrollah, B., M. Kumar, and T. E. Link (2013), On the role of vegetation density on net snow cover radiation at the forest floor, *J. Geophys. Res. Atmos.*, 118, doi:10.1002/jgrd.50575.

1. Introduction

[2] Snow cover ablation is an important process that affects hydrologic states and fluxes and water resources including groundwater recharge, stream-aquifer interactions, water quality, urban and agricultural water supply, and hydropower generation [Lundquist and Flint, 2006; Stewart *et al.*, 2005]. Decrease in snowpack amount and alteration of melt timing may disrupt agricultural and municipal water supplies [Rango and Vankatwijk, 1990; Varhola *et al.*, 2010; Winkler and Roach, 2005]. Alteration of canopy cover may either increase or decrease the timing and rate of snowmelt depending on slope and aspect [Ellis *et al.*, 2011], and seasonal climate conditions (J. D. Lundquist, S. E. Dickerson-Lange, J. A. Lutz, and N. C. Cristea, Temperature-induced tipping point in net effect of forests on snowmelt, *Water Resour. Res.*, in review, 2013). One of the primary factors that influence snow

energetics is the net snow cover (as an emitter and reflector) radiation [Aguado, 1985; Bohren and Thorud, 1973; Elder *et al.*, 1991], which typically is the dominant energy flux component when turbulent fluxes are relatively small, even in forests [Link and Marks, 1999]. Prediction of snowmelt in forested settings therefore necessitates understanding and prediction of the spatial and temporal distribution of net radiation on the forest floor [Varhola *et al.*, 2010].

[3] Net snow cover radiation on the forest floor (NSRF) depends on a wide range of environmental and physical parameters including solar angles (controlled by latitude and time), vegetation density and geometry, physical properties of snow and canopy such as albedo and longwave emissivity, air temperature, humidity, sky cover, and local slope and aspect [Flerchinger *et al.*, 2009; Gelfan *et al.*, 2004; Kaminsky and Dubayah, 1997; Kumar *et al.*, 1997; Marthews *et al.*, 2012; Pomeroy *et al.*, 2009]. NSRF consists of multiple radiation components which can be broadly classified into two spectral bands: longwave (3.5–100 μm) radiation from trees, sky and snow, and shortwave (0.28–3.5 μm) radiation that includes direct beam and diffuse radiation, and reflected shortwave from snow on the ground [Link and Marks, 1999; Pomeroy and Dion, 1996; Pomeroy *et al.*, 2009] and canopy [Bohren and Thorud, 1973]. Several studies have evaluated individual radiation components and explored the influence of different environmental and physical variables. Longwave

¹Nicholas School of the Environment, Duke University, Durham, North Carolina, USA.

²College of Natural Resources, University of Idaho, Moscow, Idaho, USA.

Corresponding author: M. Kumar, Nicholas School of the Environment, Duke University, Durham, NC 27708, USA. (mukesh.kumar@duke.edu)

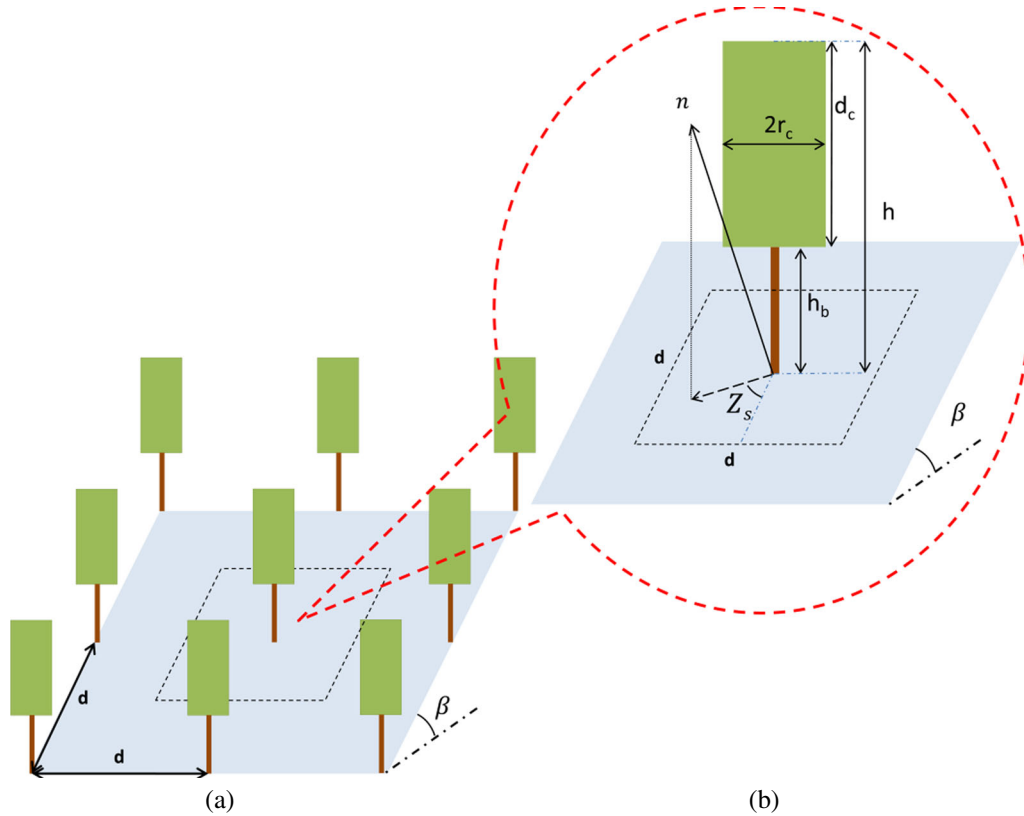


Figure 1. (a) Gridded arrangement of trees on a forested hillslope; (b) control volume and tree geometry where h is tree height, r_c is crown radius, d_c is crown depth, h_b is tree base height, β is slope angle, Z_s is the surface azimuth angle, d is distance between trees, and n is surface normal vector.

radiation is predominantly controlled by temperature and emissivity of the source [Awanou, 1998]. Net longwave radiation on the forest floor is influenced by the contribution of radiation from multiple sources including canopy [Gay, 1968; Gay et al., 1971; Pomeroy et al., 2009], sky [Pluss and Ohmura, 1997], and emitted longwave radiation from the snowpack [Male and Granger, 1981]. The above-canopy incoming shortwave radiation varies with solar zenith angle which depends on latitude, season, time of day, and atmospheric turbidity [Male and Granger, 1981]. In forested settings, the above-canopy radiation declines as it passes through the canopy depending on the size and location of canopy gaps, canopy leaf area [Hardy et al., 2004], leaf orientation [Monteith and Unsworth, 2008], foliage density in the crown [Hutchison and Matt, 1977], and tree geometry including height, shape, and crown base height [Davis et al., 1997; Rasmus et al., 2011]. The shortwave radiation reaching the forest floor is also modulated by topographic factors such as elevation, slope, aspect, and adjacent terrain shading [Dubayah and Rich, 1995; Ellis et al., 2011; Gustafson et al., 2010; Hendrick et al., 1971; Jost et al., 2007; Kumar et al., 1997]. Net shortwave radiation is also influenced by snow albedo which determines the amount of reflected shortwave radiation [Link and Marks, 1999].

[4] Evaluation of net radiation for a range of vegetation densities (from sparse to very dense forests) is challenging. Most of the efforts related to quantification of NSRF in relation to discontinuous vegetation cover have focused on conditions in isolated canopy gaps [Berry and Rothwell,

1992; Gary, 1974; Golding and Swanson, 1978; Lawler and Link, 2011] or on comparison of radiation between open and relatively homogeneous stands with a limited range of tree densities [Hardy et al., 1997; Musselman et al., 2008; Price and Dunne, 1976; Sicart et al., 2004]. Only a limited number of efforts have evaluated how variations in vegetation density influence net snow cover radiation under forest canopies [Bohren and Thorud, 1973; USACE, 1956]. An analytical model used to explore how the variation in net radiation changes with respect to vegetation density in conifer forests showed existence of a maximum net radiation for high snow albedos. For other snow albedo ranges, the relationship was found to be either monotonically increasing or decreasing [Bohren and Thorud, 1973]. In contrast, a study in a lodgepole pine forest at $\sim 39^\circ\text{N}$ latitude reported that incoming net radiation in forested areas had a minimum value at an intermediate vegetation density [USACE, 1956]. While the aforementioned research highlights the disparate relationships between snow-covered forest floor radiation to vegetation density, the controls on these relationships in relation to spatial and temporal variations of different radiation components in forested settings have not been fully quantified. Furthermore, influences of topographic characteristics such as slope and aspect on the radiation trends spanning a range of forest densities have not been evaluated.

[5] The primary goal of this research is to quantify and understand the controls on net radiation in relation to vegetation density for different slopes and aspects. To understand

Table 1. Input Parameters Used in the Model

Quantity	Value
Snow albedo for diffuse radiation (α_{dif})	0.8
Snow albedo for direct radiation (α_{dir})	0.4
Snow free canopy albedo (α_c)	0.2
Snow emissivity (ϵ_{snow})	1.0
Canopy emissivity (ϵ_{can})	0.98
Crown and air temperature difference in dense forests ($T_{\text{crown}} - T_{\text{air}}$)	0.5°C
Crown and air temperature difference in sparse forests ($T_{\text{crown}} - T_{\text{air}}$)	1.5°C
Trunk and air temperature difference in dense forests ($T_{\text{trunk}} - T_{\text{air}}$)	10°C
Trunk and air temperature difference in sparse forests ($T_{\text{trunk}} - T_{\text{air}}$)	20°C

the relative contribution of different radiation components reaching the forest floor, here we present a physically based forest radiation model (FoRM) that uses discrete representations of individual trees. In this study, the model is used to predict spatially distributed radiation components in a gridded infinite forest; however, the model formulation is also generic enough to be applied for NSRF calculation within heterogeneous forest patches. FoRM can be run at relatively fine temporal scales (e.g., < 1 h) and can therefore be used to assess the temporal variability of all radiative energy components ranging from daily to seasonal scales and across a range of spatial scales ranging from the tree (e.g., < 1 m) to the stand (e.g., > 10 m) level. Specifically, four questions using FoRM are addressed in this work: (a) How does vegetation density influence net radiation on the forest floor during clear sky conditions? (b) How does sky cloudiness alter the variation of net radiation for different vegetation densities? (c) How does slope affect the amount of net radiation for a range of vegetation densities in relation to horizontal sites? and (d) How does aspect affect the amount of radiation for a range of vegetation densities?

2. FoRM: A Forest Radiation Model

[6] Numerical experiments were designed to understand the variation of radiation below a coniferous forest canopy for both flat and inclined topography. The analysis was performed using virtual trees with cylindrical shaped crowns that are typical of white spruce (*Picea glauca*) [Gilman and Watson, 1994]. The species represents a relatively common conifer tree that is widely distributed in Northern Hemisphere forests that extend from 43° (Maine) to 69° north latitude (Alaska) [MFC, 1908; plantmaps.com, 2012] and hence was selected as a generic conifer for these investigations. FoRM accounts for modification of radiation at the forest floor due to a number of tree morphometric characteristics including height, shape, crown diameter and density, and crown base height. For simplicity, the forest was assumed to have a homogeneous gridded tree distribution, with distance between trees being equal to d . To evaluate the variation of NSRF for changing vegetation density, d was varied between experiments. Because of the symmetric arrangement and infiniteness of the forest, NSRF in each rectangular ($d \times d$) control volume, with a tree at its center (Figure 1), is the same as the average NSRF for the whole forest.

[7] Net radiation on the forest floor (R_{Net} in W m^{-2}) is modeled as a sum of net longwave (L_{Net} in W m^{-2}) and shortwave (S_{Net} in W m^{-2}) radiation components within the

control volume [Hardy et al., 1997; Pomeroy et al., 2009; Sicart et al., 2006]:

$$R_{\text{Net}} = L_{\text{Net}} + S_{\text{Net}}. \quad (1)$$

[8] Net radiation is positive if the radiant flux is toward the snow cover. The spatiotemporal average of net radiation, $\langle \text{NSRF} \rangle$ (W m^{-2}), on the forest floor is calculated using

$$\langle \text{NSRF} \rangle = \frac{\int_{t_1}^{t_2} \int_{-d/2}^{+d/2} \int_{-d/2}^{+d/2} R_{\text{Net}} dx dy dt}{(t_2 - t_1) d^2}, \quad (2)$$

where d is distance between trees. The radiation calculation is performed between winter (t_1) and summer (t_2) solstices in each control volume. The simulation period spans the entire duration of the snow season for many coniferous forests in mountain environments. It is assumed that snow exists on the forest floor for the entire snow season. Notably, the analyses can be performed for any place- and year-specific snow cover duration.

[9] Net snow cover longwave radiation expands to

$$L_{\text{Net}} = \downarrow L_{\text{sky}} + \downarrow L_{\text{crown}} + \downarrow L_{\text{trunk}} - \uparrow L_{\text{snow}}, \quad (3)$$

where $\downarrow L_{\text{crown}}$ is incoming longwave radiation from tree crowns (W m^{-2}), $\downarrow L_{\text{trunk}}$ is incoming longwave radiation from tree trunks (W m^{-2}), $\downarrow L_{\text{sky}}$ is incoming longwave radiation from sky (W m^{-2}), and $\uparrow L_{\text{snow}}$ is outgoing longwave radiation from snow (W m^{-2}). The four longwave radiation components (see equation (3)) are computed using the Stefan-Boltzmann equation. The canopy, trunk, and sky longwave irradiances are estimated from the temperatures and emissivities of respective sources using equations (4), (5), and (6) [Essery et al., 2008a; Gryning et al., 2001; Male and Granger, 1981; Marks and Dozier, 1979; Pluss and Ohmura, 1997; Pomeroy et al., 2009; Sicart et al., 2006; Todhunter et al., 1992].

$$\downarrow L_{\text{sky}} = \text{SVF} \sigma \epsilon_{\text{sky}} T_{\text{air}}^4, \quad (4)$$

$$\downarrow L_{\text{trunk}} = \text{TVF} \sigma \epsilon_{\text{can}} T_{\text{trunk}}^4, \quad (5)$$

$$\downarrow L_{\text{crown}} = (1 - \text{SVF} - \text{TVF}) \sigma \epsilon_{\text{can}} T_{\text{crown}}^4, \quad (6)$$

where SVF is the sky view factor, TVF is the trunk view factor, σ is Stefan-Boltzmann constant ($\sigma = 5.67 \times 10^{-8} \text{ W m}^{-2} \text{ K}^{-4}$), ϵ_{sky} is sky emissivity, T_{air} is air temperature (K), ϵ_{can} is the canopy emissivity for both crown and trunk, T_{crown} is crown temperature (K), and T_{trunk} is trunk temperature (K). Generally, air temperature is a good estimate of crown temperature in low-insolation conditions and under relatively dense canopies during high insolation [Pomeroy et al., 2009]. However, needle and branch temperatures can exceed air temperature by about 1–2 K in low-density canopies during high-insolation conditions. Trunk temperatures can be even larger, with magnitudes as high as 20 K higher than air temperature during high-insolation conditions and around 10 K higher during low-insolation conditions [Pomeroy et al., 2009]. In the absence of any supporting data at intermediate densities, the observed temperature differences for discontinuous and dense forests from Pomeroy et al. [2009] are used for calculation of differences between air and crown/trunk temperatures at intermediate vegetation densities (Table 1). Since shortwave radiation is a dominant control in determining how warm canopies and trunks are in relation to air temperature, observed

Table 2. Location and Characteristics of the Sites Used in the Model

Site Location	Data Set	Site Characteristics
NCDC site at Greenville, ME (1977–2012)	Air temperature and relative humidity	Latitude: 45.5°N Longitude: 69.6°W Elevation: 423 m Annual mean temperature: 4.9°C Annual temperature range: 28.3°C Diurnal temperature range: 9.2°C
NREL site at Millinocket, ME (1990–2010)	Solar radiation and sky cover	Latitude: 45.6°N Longitude: 68.7°W Elevation: 124 m Annual mean sky cover: 56.1 %
LSOS site at Fraser, CO	Validation of shortwave and longwave radiation data	Latitude: 39.9°N Longitude: 105.9°W Elevation: 2780 m

temperature differences at Fraser Experimental Forest near Fraser, Colorado, U.S. (39.9°N, 105.9°W) [Pomeroy *et al.*, 2009] for the two defined vegetation density extremes were regressed against modeled shortwave radiation at intermediate vegetation densities to obtain the variation of crown/trunk temperature differences with vegetation density. Additionally, sky and snow temperatures are assumed to be uniformly distributed across the control volume. Outgoing longwave radiation from snow on the forest floor to the atmosphere and tree is calculated based on [Gryning *et al.*, 2001; Todhunter *et al.*, 1992]

$$\uparrow L_{\text{snow}} = \sigma \varepsilon_{\text{snow}} T_{\text{snow}}^4, \quad (7)$$

where $\varepsilon_{\text{snow}}$ is snow emissivity (dimensionless) and T_{snow} is snow temperature (K). Snow surface emissivity is considered to be equal to 1.0 [Male and Granger, 1981], while no reflection of the longwave components from the snow surface is considered. In the analysis, snow temperature is set to dew point temperature (Tdp) when Tdp < 0°C and to zero otherwise.

[10] The incoming shortwave flux incident at the snow surface consists of two components, a direct beam, $\downarrow S_{\text{dir}}$ (W m^{-2}), and a diffuse component, $\downarrow S_{\text{dif}}$ (W m^{-2}), while $\uparrow S_{\text{snow}}$ is outgoing shortwave radiation from snow (W m^{-2}). As the direct beam passes through the atmosphere and canopy, it is attenuated by both absorption and scattering processes. Direct shortwave radiation on the forest floor is evaluated using a probabilistic approach [Nilson, 1971] and is calculated based on [Essery *et al.*, 2008b]

$$\downarrow S_{\text{dir}} = S_{\text{dir,open}} \cos(\theta) P, \quad (8)$$

$$P = e^{-G \lambda L_{\text{path}}}, \quad (9)$$

where P is the probability of a light beam not intersecting a canopy element; $S_{\text{dir,open}}$ is direct shortwave radiation for open sky (W m^{-2}) which depends on time and site latitude, slope, and aspect [Kalogirou, 2009; Kumar *et al.*, 1997]; θ is the solar incidence angle (the angle between the Sun and normal to the surface); G is the projection coefficient of leaf orientation (dimensionless); λ is the effective foliage area volume density (m^{-1}); and L_{path} is the length of the solar beam passing through the canopy (m). Assuming a random

orientation of leaves, G is assumed to equal to 0.5 in this analysis. Open sky solar radiation at the land surface varies with solar zenith angle and changes in solar distance during a year and is influenced by latitude, slope, and aspect. Open sky direct solar radiation is calculated using [Kreith and Kreider, 2011]

$$S_{\text{dir,open}} = S_{\text{extr}} \tau_b, \quad (10)$$

where S_{extr} is extraterrestrial solar radiation and τ_b is the atmospheric transmittance for beam radiation. For clear sky conditions, atmospheric transmittance is calculated using [Hottel, 1976]

$$\tau_b = a_0 + a_1 e^{-\frac{k}{\cos \psi}}, \quad (11)$$

$$a_0 = 0.4237 - 0.00821(6 - A)^2, \quad (12)$$

$$a_1 = 0.5055 + 0.00595(6.5 - A)^2, \quad (13)$$

$$k = 0.2711 + 0.01858(2.5 - A)^2, \quad (14)$$

where ψ is solar zenith angle; a_0 , a_1 , and k are constant coefficients; and A is the altitude of the site in kilometers. Extraterrestrial solar radiation and its variation with location and time is evaluated based on Kalogirou [2009] and is presented in Appendix A. Diffuse shortwave radiation due to scattering is calculated based on [Essery *et al.*, 2008b; Kumar *et al.*, 1997]

$$\downarrow S_{\text{dif}} = \text{SVF} S_{\text{extr}} \tau_d \cos \psi \cos^2(\beta/2), \quad (15)$$

where β is the slope and τ_d is the atmospheric diffusion factor. Considering that τ_d is a linear function of τ_b [Wong and Chow, 2001], a regression equation was derived from available data of clear sky days at the closest National Renewable Energy Laboratory site [NREL, 2012] in Maine (Table 2), to estimate τ_d in clear sky conditions:

$$\tau_d = 0.312 - 0.304\tau_b. \quad (16)$$

[11] For cloudy sky conditions, τ_d and τ_b are directly extracted from NREL data by comparing diffuse and direct beam radiation with extraterrestrial radiation. Snow on the forest floor reflects a fraction of incoming direct and diffuse shortwave radiation and is calculated using [Hardy *et al.*, 1997; Hardy *et al.*, 2004; Todhunter *et al.*, 1992]

$$\uparrow S_{\text{snow}} = \alpha_{\text{dif}} \downarrow S_{\text{dif}} + \alpha_{\text{dir}} \downarrow S_{\text{dir}}, \quad (17)$$

where α_{dif} and α_{dir} are snow albedo (dimensionless) for diffuse and direct radiation, respectively. Taking into account the infinitely many reflections of shortwave radiation between the snow-covered forest floor and canopy [Bohren and Thorud, 1973], net shortwave radiation (S_{Net}) is calculated as

$$S_{\text{Net}} = \frac{\downarrow S_{\text{dir}}(1 - \alpha_{\text{dir}})}{1 - \alpha_{\text{dir}}\alpha_c(1 - \text{SVF})} + \frac{\downarrow S_{\text{dif}}(1 - \alpha_{\text{dif}})}{1 - \alpha_{\text{dif}}\alpha_c(1 - \text{SVF})}, \quad (18)$$

where α_c is canopy albedo. Notably, two variables that change with vegetation density and have a large effect on NSRF are sky view factor (SVF) and path length (L_{path}). Sky view factor affects longwave radiation from the tree crowns, trunks, and sky, and diffuse shortwave radiation from the sky. Assuming that canopy structure is invariant throughout the year, SVF is only a function of location

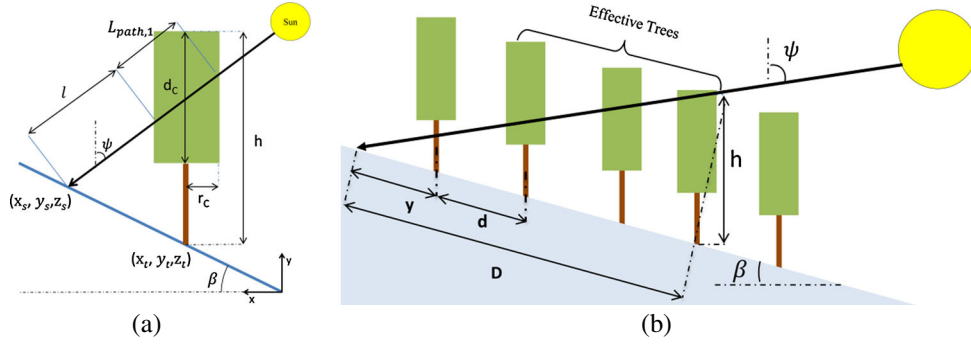


Figure 2. (a) Path length calculation on the forest floor; (b) effective number of trees considered for path length calculation at any point on the forest floor.

within a stand. Path length influences direct shortwave radiation. Since path length changes with the solar zenith angle and azimuth, $\downarrow S_{dir}$ and S_{Net} vary both spatially and temporally.

2.1. Path Length

[12] The spatiotemporal distribution of path length is calculated using a ray-tracing method similar to the one discussed in *Essery et al.* [2008b] where path length calculations were performed for ellipsoidal crown shapes at a level site. Here, the formulation is extended to account for inclined topography and cylindrical tree shapes to represent a generic, yet physically reasonable, coniferous tree form. Path length, L_{path} , is obtained by calculating the absolute difference between two positive solutions of the parametric equation representing a cylindrical crown (Figure 2a). The parametric equation for the cylindrical crown form is represented by

$$\frac{(x - x_t)^2 + (y - y_t)^2}{r_c^2} = 1, h_b \leq z \leq h, \quad (19)$$

where (x_t, y_t) is the coordinate of the stem, h is tree height, h_b is crown base height, and r_c is crown radius. A quadratic equation for l is obtained by replacing $x, y,$ and z in equation (19) with

$$x = x_s + l \sin\psi \sin(Z - Z_s), \quad (20)$$

$$y = y_s \cos\beta - l \sin\psi \cos(Z - Z_s), \quad (21)$$

$$z = l \cos\psi + y_s \sin\beta, \quad (22)$$

where Z and Z_s are the solar and surface azimuth angles, respectively. Equation (19) reduces to

$$a^2 + bl + c = 0, \quad (23)$$

where $a, b,$ and c are

$$a = \frac{\sin^2\psi}{r_c^2}, \quad (24)$$

$$b = \frac{2 \sin\psi (\cos(Z - Z_s)(y_t - y_s \cos\beta) + (x_s - x_t) \sin(Z - Z_s))}{r_c^2}, \quad (25)$$

$$c = \frac{-r_c^2 + (x_s - x_t)^2 + y_t^2 + y_s \cos\beta (-2y_t + y_s \cos\beta)}{r_c^2}. \quad (26)$$

[13] The discriminant of equation (23) is defined as

$$\Delta = b^2 - 4ac. \quad (27)$$

[14] The path length for a single tree, $L_{path,1}$, is the difference between two solutions of the quadratic equation and is calculated as

$$L_{path,1} = \begin{cases} \frac{\sqrt{\Delta}}{a} & \Delta > 0 \\ 0 & \Delta \leq 0 \end{cases} \quad (28)$$

[15] In a forested setting, path lengths have to be calculated to account for the passage of beam radiation through multiple crowns. Total path length (Figure 2b) is calculated at any location by adding path lengths through multiple crowns using

$$L_{path, crown} = \sum_{\text{if } D < h \cos\beta \tan(\psi - \beta \cos(Z - Z_s))} L_{path,1}, \quad (29)$$

where $(Z - Z_s)$ is the angle between the Sun and surface azimuths, and D is the distance shown in Figure 2b. To calculate path length through tree trunks ($L_{path,1, trunk}$), $r_c, h_b,$ and h are replaced by $r_t, 0,$ and $h_b,$ respectively, through equations (19) to (28). Because of the nontransmissive trunks, if $L_{path,1, trunk} > 0,$ P in equation (9) equals 0.

2.2. Sky View Factor

[16] The sky view factor (SVF) is the fraction of hemispherical sky that is viewable from a given point [Matzarakis and Matuschek, 2011]. A three-dimensional approach is used to estimate sky view factor for every grid cell on the forest floor. The hemispherical sky is meshed, and each discretized element is identified in polar coordinates (angular altitude and azimuth). The hemisphere is divided into 180 intervals along the altitude direction and 360 intervals along the azimuthal direction. On the hemisphere, a cell is marked blocked if a tree lies in the line of sight to it. Area blocked by the vegetation canopy in a certain direction (φ) is identified as the subtended region between tree zenith (ω) and ground along-altitude axis and between $\varphi - d\varphi$ and

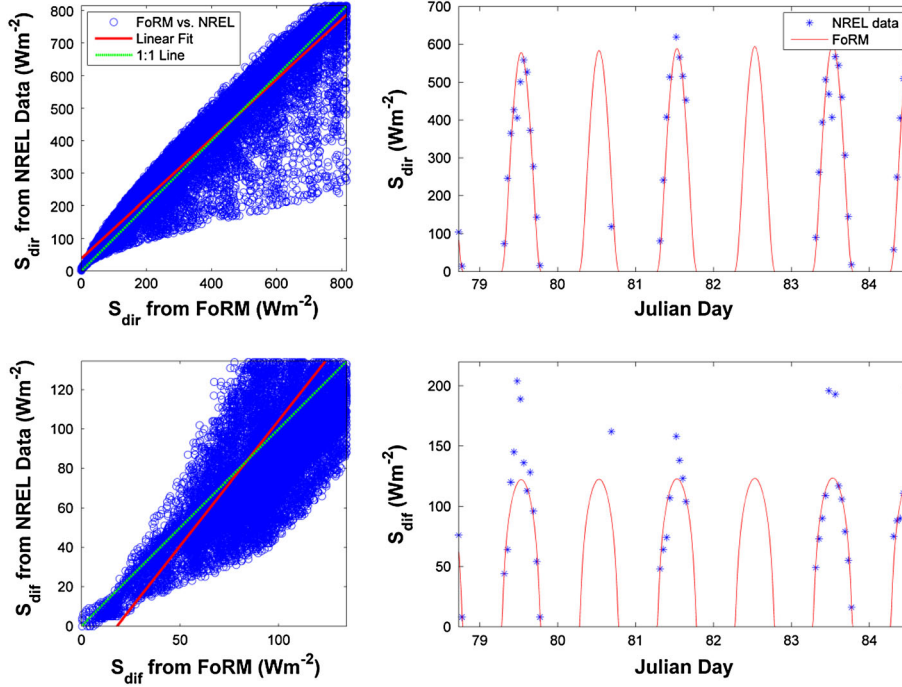


Figure 3. Modeled above-canopy direct (top) and diffuse (bottom) shortwave radiation components versus NREL radiation data at Millinocket, ME, the closest NREL site to Greenville, ME. Comparison is performed for hourly data from 1990 to 2010. R^2 for direct and diffuse comparisons are 0.91 and 0.45, respectively.

$\varphi + d\varphi$ along the azimuth. Tree zenith angle (ω) and central azimuth (φ) are calculated by

$$\varphi = \tan^{-1} \left(\frac{P_y - T_y}{P_x - T_x} \right), \quad (30)$$

$$\omega = \cos^{-1} \left(\frac{\vec{PT} \cdot \vec{PI}}{|\vec{PT}| |\vec{PI}|} \right), \quad (31)$$

where P is the location at which SVF is to be calculated, point T is the tree base, and point I is the top of the tree. Width of the area blocked by the canopy is $2d\varphi$, where $d\varphi$ is

$$d\varphi = \tan^{-1} \left[\frac{r_c}{\left((P_x - T_x)^2 + (P_y - T_y)^2 \right)^{1/2}} \right]. \quad (32)$$

[17] The sky view factor calculation also accounts for incoming radiation transmitted through the canopy. A probabilistic ray-tracing method is used to estimate the sky view factor. The probability of seeing the sky, $p(\omega, \varphi)$, for open sky pixels is 1 and for blocked pixels is $e^{-G^\lambda L(\omega, \varphi)}$. SVF is obtained by

$$\text{SVF} = \int_0^{2\pi} \int_\gamma \frac{p(\omega, \varphi)}{\pi^2} d\omega d\varphi, \quad (33)$$

where γ is directional horizon angle and obtained using

$$\gamma = \begin{cases} \sec^{-1} \left(\sqrt{1 + \cos^2 \phi \tan^2 \beta} \right) & \text{for } \pi/2 \leq \phi \leq 3\pi/2 \\ -\sec^{-1} \left(\sqrt{1 + \cos^2 \phi \tan^2 \beta} \right) & \text{otherwise.} \end{cases} \quad (34)$$

[18] Similar to SVF, trunk view factor (TVF) is calculated when only tree trunk is considered. We call this algorithm to estimate sky view factor the *SkyMap* method.

2.3. Model Application

[19] Representative values of physical parameters including $\varepsilon_{\text{snow}}$, ε_{can} , α_{dir} , α_{dif} and α_c were used to calculate individual energy components of NSRF. Typical values of snow albedo and emissivity of canopy, sky, and snow are listed in Table 1. Snow albedo has a spectral variation from 0 to 0.9 depending on snow age, grain size, and wavelength [Warren and Wiscombe, 1980; Wiscombe and Warren, 1980]. An intermediate value of 0.4, representative of the seasonal average albedo in forested settings where debris deposition from the forest canopy is common [Melloh et al., 2002], was used in this analysis. Snow albedo for diffuse radiation, α_{dif} , was set equal to 0.8 [Wang and Zeng, 2010]. Canopy albedo was set to 0.2 [Bohren and Thorud, 1973; Eck and Deering, 1990, 1992]. The emissivity of snow and canopy were set to 1.0 [Dozier and Warren, 1982; Sicart et al., 2006; Warren, 1982] and 0.98 [Pomeroy et al., 2009] respectively. Although these values for albedo and emissivity would likely differ for a given site at any given time in the snow season, they were selected as reasonable values in order to assess the relative sensitivity of snow cover net radiation to vegetation density. Clear sky emissivity depends on air temperature, pressure, and humidity [Marthews et al., 2012]. Daily clear sky emissivity ($\varepsilon_{\text{sky,clear}}$) is estimated using [Prata, 1996]

$$\varepsilon_{\text{sky,clear}} = 1 - (1 + w)e^{-\sqrt{1.2+3w}}, \quad (35)$$

where w is precipitable water in the air (cm) and calculated as

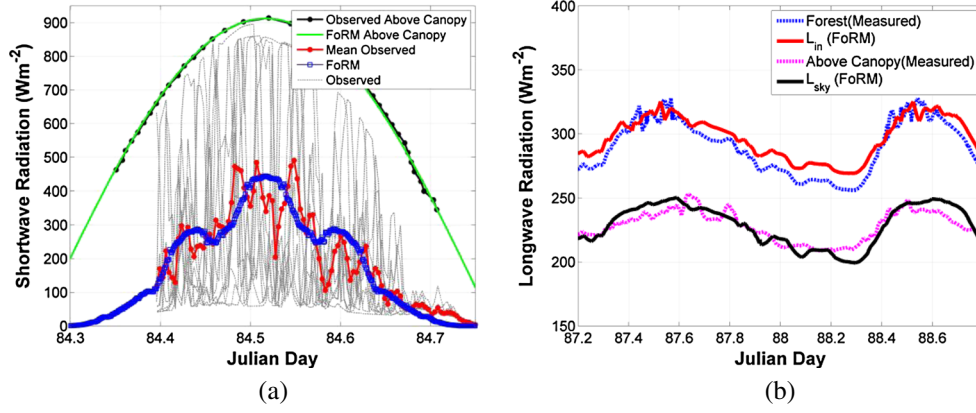


Figure 4. Modeled and measured (a) shortwave and (b) longwave radiations in the uniform lodgepole pine forest ($cc \approx 47\%$) at the Local Scale Observation Site (LSOS) in Fraser, CO, U.S.. The shortwave irradiance results are well correlated with the observation ($R^2 = 0.80$). Above and beneath the canopy, longwave radiations from the model also compare well against observation and have an R^2 of 0.81 and 0.93, respectively.

$w \approx 465 \left(\frac{e_0}{T_{\text{air}}} \right)$, e_0 is ambient vapor pressure (kPa), and T_{air} is screen-level air temperature (K). Cloudy sky emissivity ($\epsilon_{\text{sky, cloudy}}$) is obtained using Prata-Keding model, which was noted to perform particularly well for North American locations [Flerchinger et al., 2009]:

$$\epsilon_{\text{sky, cloudy}} = (1 + 0.153 C^{2.183}) \epsilon_{\text{sky, clear}}, \quad (36)$$

where C is the fraction of cloud cover.

[20] The variation of NSRF in relation to vegetation density was calculated for a white spruce forest stand near Greenville, ME (45.5°N). White spruce is a common tree species at midlatitudes to high latitudes in North America. This species is widely distributed in the boreal forest of North America ranging from mountainous areas in the west to coastal regions in the east. White spruce has a cylindrical crown shape and can grow up to 28 m in height and 6 m in width [Arbor Day Foundation, 2012; MFC, 1908]. This species and location were selected as a generic representation of midlatitude North American sites where there is considerable interest in understanding the effects of coniferous forest densities on seasonal snow energetics. In this analysis, we consider a typical tree dimension, with crown radius, r_c , being equal to 3 m; tree height, h , being equal to 24 m; and tree trunk radius, r_t , being equal to 0.4 m. The model was run using a meteorological data set such as air temperature and relative humidity from National Climatic Data Center (NCDC) meteorological station near Greenville, ME [NCDC, 2012] and cloud cover data obtained from NREL [NREL, 2012]. The site has long-term air temperature (1977–2012) and solar radiation (1990–2010) data. Relevant information about the site is listed in Table 2. Given the absence of effective foliage area volume density (λ , equation (9)) information for white spruce, λ was estimated based on allometric relationships for Engelmann spruce, which has a similar structure [Kaufmann et al., 1982]:

$$\lambda = \frac{0.975 h^2}{\pi r_c^2 d_c}, \quad (37)$$

where d_c is crown vertical depth and was assumed to be equal to 20 m. In this paper, the vegetation density is presented as

$1/d$, where d is the distance between trees. Canopy closure (cc), an alternate metric, used in the literature [Reifsnnyder and Lull, 1965] to quantify vegetation density, can be related to d as $cc = \frac{\pi r_c^2}{d^2}$.

[21] All the radiation components (equation (1)) were calculated on a 200×200 grid within a control volume (Figure 1b) for vegetation densities of $1/d$ ranging from 0.005 m^{-1} to 0.17 m^{-1} , where d is distance between trees. The average net radiation from 21 December to 20 June, calculated on 40,000 grid cells, was then used to evaluate the variation of net radiation in relation to vegetation density ($1/d$). Comparison of S_{dir} and S_{dif} from the model (equations (10) to (16)) for open clear sky conditions against NREL data, at the site closest to Greenville, ME, showed an adequate match (Figure 3, $R^2 = 0.91$ for direct radiation and $R^2 = 0.45$ for diffuse radiation). Incoming shortwave radiations obtained from FoRM were compared against observed data, both above and underneath the canopy, in a uniform lodgepole pine forest at the Local Scale Observation Site (LSOS, [NSIDC, 2013]) in Fraser, CO, U.S. (39.9°N, 105.9°W, elevation = 2780 m). Measured incoming longwave radiations at the LSOS, both above the canopy and on the forest floor, were also compared with the radiation derived from the model. Details of the shortwave and longwave radiation observation experiments can be referred in Hardy et al. [2004] and Pomeroy et al. [2009], respectively. The model was run for representative tree geometry ($h = 12.6 \text{ m}$, $d_c = 8.8 \text{ m}$, $r_c = 1.38 \text{ m}$, $r_t = 0.18 \text{ m}$) and canopy closure ($cc = 47\%$, $d = 0.28 \text{ m}^{-1}$) at the site. Although shortwave radiation shows a strong spatial gradient at the site, the modeled shortwave radiation reasonably reproduces both the temporal trend ($R^2 = 0.80$) and integrated mean observed data (1.5% difference in the total energy received at the forest floor, Figure 4a). The comparisons of longwave radiations between the model and the observations also show satisfactory correlations ($R^2 = 0.81$ for above the canopy and $R^2 = 0.93$ for the forest floor). Moreover, the difference of total longwave radiations as estimated by the model and the observations are minuscule (0.6% for above the canopy and 1.2% at the forest floor, Figure 4b).

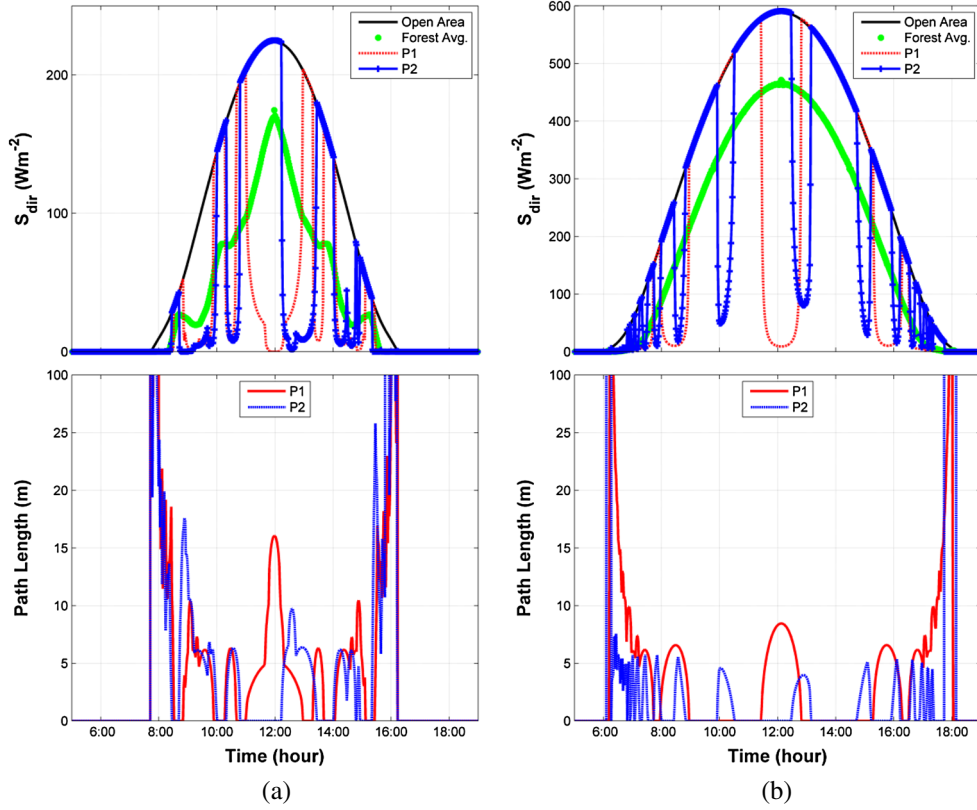


Figure 5. Daily variation of direct shortwave radiation and path length for $1/d \approx 0.04 \text{ m}^{-1}$ on (a) 21 December and (b) 20 March. Points P1 and P2 refer to the locations shown in Figure 6.

Due to logistical challenges associated with the measurement of distributed radiation across a range of vegetation densities, especially for different slopes and aspects, net shortwave radiation for a range of vegetation densities remain unvalidated. It is to be noted that the equations used to calculate the individual radiation components in FoRM have been previously validated in the referenced literature and given the acceptable validation at control sites; this model is considered to be reasonable to advance insight into the controls of vegetation density on net snow cover radiation.

3. Results and Discussion

[22] The results are presented thematically, following the questions outlined previously.

3.1. Vegetation Density Influence on Net Radiation at the Forest Floor for Clear Sky Conditions

[23] The spatiotemporal variation in $\downarrow S_{\text{dir}}$ is primarily due to variation in $S_{\text{dir,open}}$ and shading fractions. Figure 5 shows the temporal variation in S_{dir} at two orthogonal points on the forest floor (P1, P2) that are located at a distance of $d/2$ and $d/4$, respectively, from a tree in the spatial domain shown in Figure 6. The two points provide information about the spatiotemporal variation in radiation for a relatively sparse forest at locations that are at distinct distances and directions from an individual tree. $\downarrow S_{\text{dir}}$ at these two points is equal to $S_{\text{dir,open}}$, unless they are shaded. The magnitude of $\downarrow S_{\text{dir}}$ in shaded regions is dependent on path length (L_{path}), which changes with Sun angle and tree spacing. As the number

of trees along the direct beam path increases, L_{path} also increases, and hence $\downarrow S_{\text{dir}}$ is less due to absorption and scattering by the canopy. For example, P1 is shaded around noon, by both the center tree and the tree directly south of it (see Figure 6). As a result, over time, the path length first increases due to the solar beam passing through one tree crown and then through two tree crowns, resulting in a dome-shaped variation in L_{path} that peaks at solar noon (Figure 5a). For the same period, $\downarrow S_{\text{dir}}$ at P2 is markedly different. Notably, during early and late hours of the day when the Sun is closer to the horizon, L_{path} increases to a very high value at both P1 and P2 (Figures 5a and 5b). Both increase in $\downarrow S_{\text{dir}}$ and decrease in shading fraction contribute to an increasing trend in net shortwave radiation with decreasing solar zenith angle on a flat forest floor. The phenomenon is evident in Figure 6 where in the morning of 21 December (9:00 A.M. local standard time), shadows are relatively long and oriented in the northwest direction. At this time, 69% of the control volume basal area is shaded, and the ratio of average shortwave radiation in the forest to an open area, or forest transmissivity (τ), is about 37%. At noon, tree shadows are smaller, hence the shading fraction is only 25% of the control volume area, and $\tau = 76\%$. In the afternoon (2:00 P.M. local standard time), tree shadows start increasing again and shading fraction increases to 62% of the control volume area. In this case, τ reduces to 46%. For the same time of the day in spring, shading fraction is lesser and forest transmissivity is greater, relative to the winter, due to higher Sun angles (Figure 6).

[24] Irrespective of the timing, shading fraction on the forest floor increases with increasing vegetation density

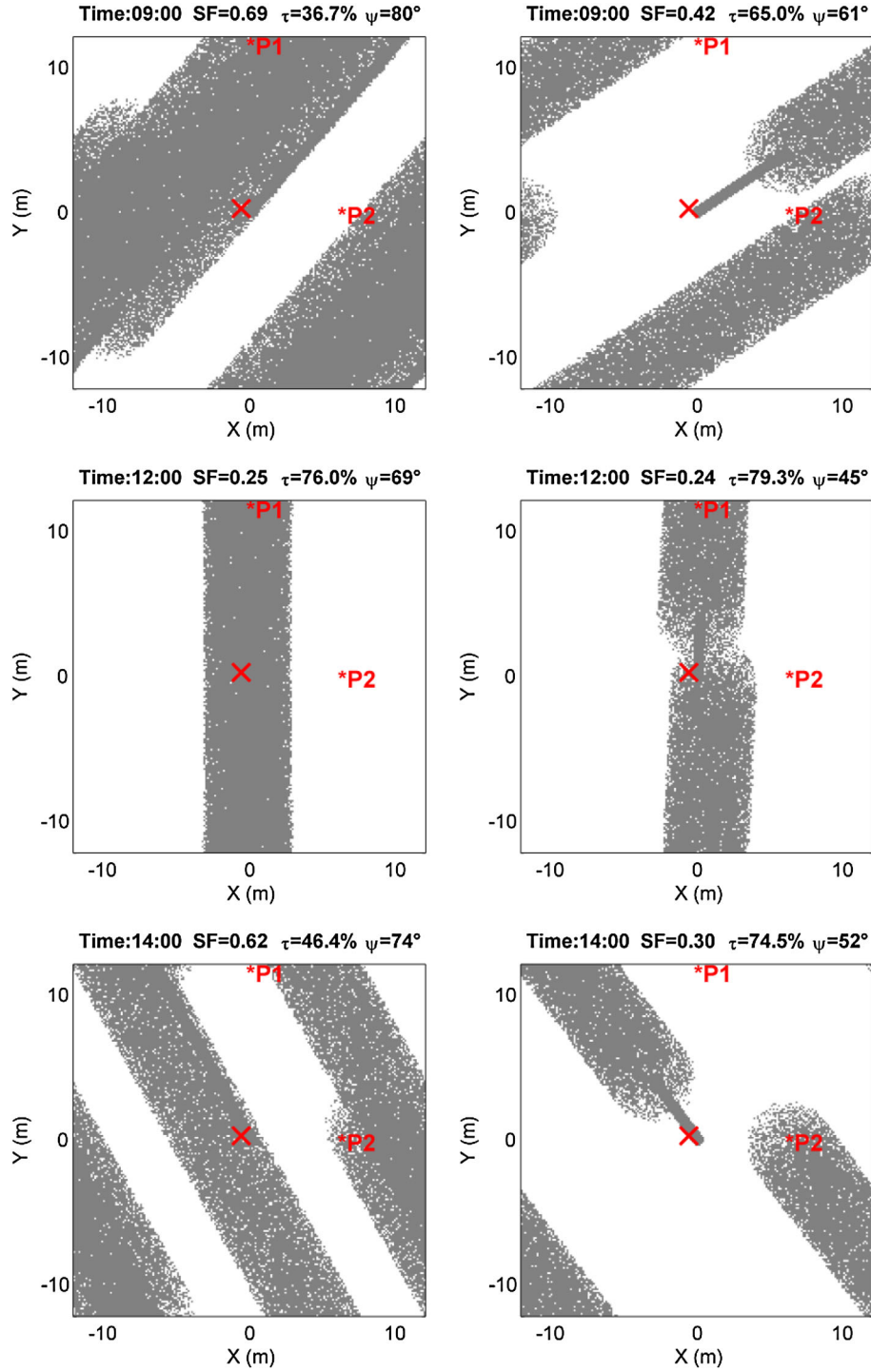


Figure 6. Shadow pattern at three times on (left) 21 December and (right) 20 March; ($1/d \approx 0.04 \text{ m}^{-1}$; tree position is marked by the cross; SF: shading fraction; τ : canopy transmissivity; ψ : solar azimuth angle).

(larger $1/d$), hence $\downarrow S_{\text{dir}}$ decays monotonically with increasing $1/d$ (Figure 7a). Increase in $1/d$ also leads to a decrease in sky view factor. Therefore, $\downarrow S_{\text{dif}}$ also decreases in high-density forests (equation (14)). The outgoing shortwave radiation component, $\uparrow S_{\text{snow}}$, also decreases with increasing $1/d$, as it is proportional to the summation of $\downarrow S_{\text{dif}}$ and $\downarrow S_{\text{dir}}$ (equation (17)). As both incoming shortwave components and the proportional outgoing component exhibit a monotonic decreasing

trend with vegetation density, S_{Net} decreases with increasing $1/d$ as expected (Figure 7b).

[25] The three longwave components vary differently in relation to vegetation density. $\downarrow L_{\text{sky}}$ varies inversely with $1/d$. This is because $\downarrow L_{\text{sky}}$ is directly proportional to the sky view factor that decreases with a denser tree spacing. On the other hand, $\downarrow L_{\text{crown}}$ and $\downarrow L_{\text{trunk}}$ increase in denser forests. Because of the higher emissivity of the canopy and trunk relative to the sky,

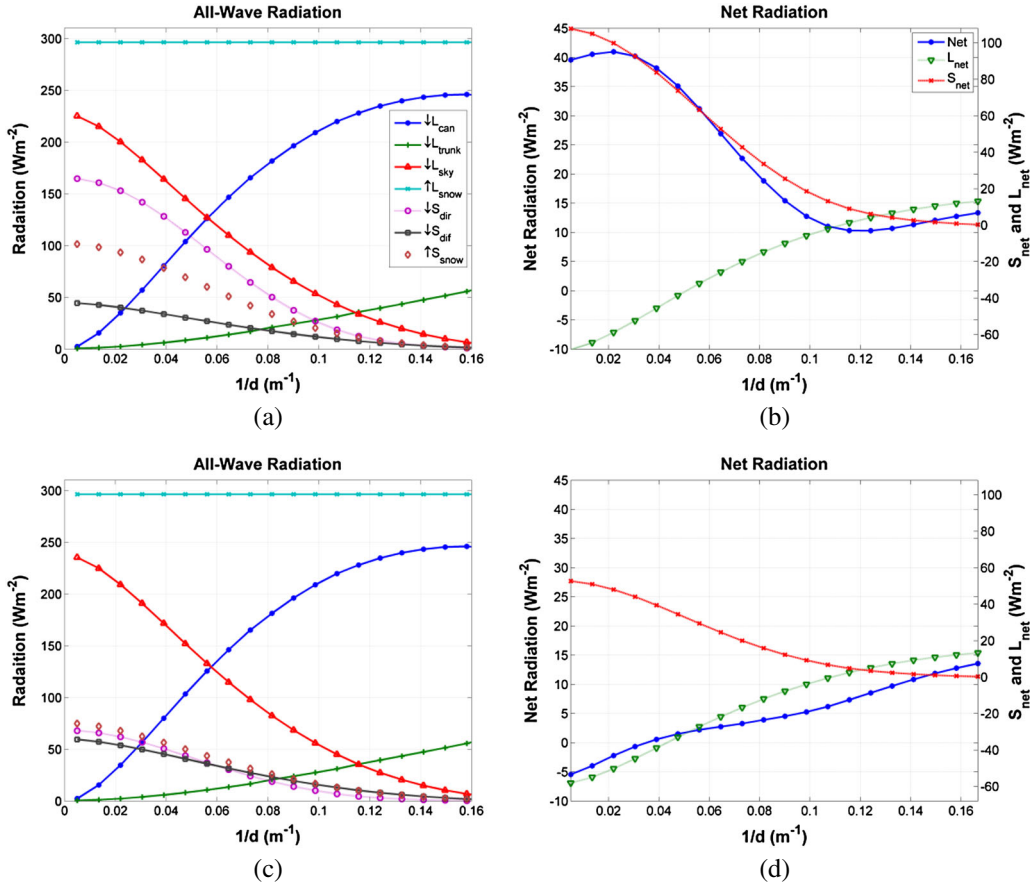


Figure 7. (a) Radiative energy components for a level forest floor in clear sky conditions, (b) net energy components for a level forest floor in clear sky conditions, (c) radiative energy components for a level forest floor in interspersed clear and cloudy sky conditions, and (d) net energy components for a level forest floor in interspersed clear and cloudy sky conditions. Note the different scales for net all-wave, shortwave, and longwave components on y axis. All radiation values are spatially as well as temporally averaged over the winter to summer solstices period.

longwave radiation from trees ($\downarrow L_{\text{tree}} = \downarrow L_{\text{crown}} + \downarrow L_{\text{trunk}}$) in very dense forests ($\text{SVF} \rightarrow 0$) is greater than $\downarrow L_{\text{sky}}$ in the open area ($\text{SVF} = 1$), and L_{Net} (see equation (3)) therefore increases with $1/d$, as expected (Figure 7b).

[26] The increasing L_{Net} and decreasing S_{Net} trends with $1/d$ leads to an interesting variation in NSRF. Due to a small shading fraction at very low vegetation densities ($1/d < 0.02 \text{ m}^{-1}$ or $cc < 2\%$), the rate of decrease in S_{Net} is relatively less than the rate of increase in L_{Net} . Therefore, the maximum NSRF occurs for very sparse forests ($1/d \approx 0.02 \text{ m}^{-1}$ or $cc \approx 2\%$) and is around 5% more than in open areas; however, for forests with density $1/d > 0.02 \text{ m}^{-1}$ ($cc > 2\%$), NSRF exhibits a different trend with changing vegetation density. In sparser forests (lower $1/d$) where S_{Net} is relatively large and L_{Net} is negative, NSRF decreases in relation to $1/d$. In denser forests (higher $1/d$), S_{Net} is negligible and NSRF increases with increase in L_{Net} as vegetation density further increases. As a result, NSRF is minimum for intermediate forest densities ($1/d \approx 0.12 \text{ m}^{-1}$ or $cc \approx 40\%$) for clear sky conditions. At the minima, NSRF is about 74% less than the open areas and 23% less than very dense forests ($1/d > 0.16 \text{ m}^{-1}$ or $cc > 75\%$). Occurrence of a minimum in intermediately dense forests with about 40% canopy closure ($1/d \approx 0.12 \text{ m}^{-1}$) is similar to results derived from an empirical

model in lodgepole pine forests in California $\sim 39^\circ\text{N}$ [USACE, 1956] and the reported results for a coniferous forest in Oregon $\sim 44^\circ\text{N}$ [Reifsnnyder and Lull, 1965].

[27] The noted trends of net radiation and magnitude of optimal vegetation densities that minimize NSRF obtained here are dependent on the time period of analysis and the representative values of parameters (e.g., snow albedo) used in the radiation calculations. Notably, since both $\downarrow L_{\text{sky}}$ and $\downarrow L_{\text{tree}}$ ($= \downarrow L_{\text{crown}} + \downarrow L_{\text{trunk}}$) vary with the fourth power of T_{air} , the relative contribution of L_{Net} and S_{Net} is dependent on T_{air} . As a result, the variation of both NSRF with $1/d$ and the density at which NSRF is minimized, is also dependent on T_{air} . Considering all other parameters to be the same, increase in average air temperature for the site will increase L_{Net} . Increase in L_{Net} due to temperature effects is higher in dense forests than sparse forests (because of $\varepsilon_{\text{sky}} < \varepsilon_{\text{can}}$), resulting in the occurrence of the NSRF minima at lower vegetation densities (Figure 8a). The results are also affected by the assumption of clear sky conditions during the entire snow season. Although the majority of the radiation during the analysis period is received during late spring and early summer which are generally characterized by clear days, a large number of cloudy days will increase the sky emissivity and

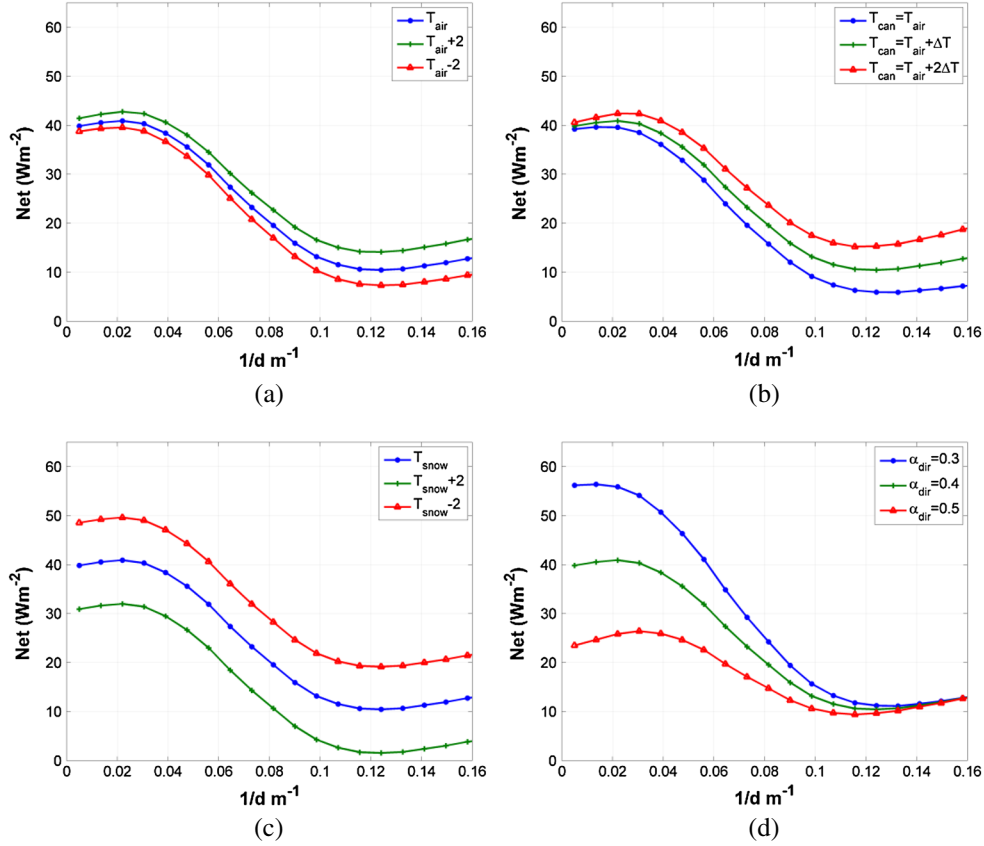


Figure 8. Sensitivity of NSRF in clear sky conditions to (a) air temperature, (b) canopy (crown and trunk) temperature, (c) snow temperature, and (d) snow albedo. In all figures, the middle curve is the representative of the obtained results in this research. All radiation values are averaged over the winter to summer solstices period.

L_{Net} and decrease incoming shortwave radiation and S_{Net} . In this scenario, the minimum NSRF may occur at a very low vegetation densities followed by a monotonic increasing trend with vegetation density which is discussed in section 3.2. Differences may also be expected for different canopy and trunk temperatures. For warmer canopy and trunk temperatures, with temperature difference to air temperature being twice of what was considered in the base simulation, the increase in L_{Net} is larger in very dense forests ($\Delta L_{\text{Net}} \approx +6 \text{ W m}^{-2}$) rather than very sparse forests ($\Delta L_{\text{Net}} \approx +0.5 \text{ W m}^{-2}$), resulting in a marginal decrease in the optimal density where radiation to snow is minimized. For colder canopy and trunk ($T_{\text{can}} = T_{\text{air}}$) conditions, L_{Net} changes with the similar trend but in the opposite direction ($\Delta L_{\text{Net}} \approx -6 \text{ W m}^{-2}$ in very dense forests and $\Delta L_{\text{Net}} \approx -0.5 \text{ W m}^{-2}$ in very sparse forests), leading to a higher optimal density. Due to gradual changes in ΔL_{Net} from low to high densities, changes in the optimal density with T_{can} are negligible (Figure 8b). Differences in snow temperature (δT_{snow}) affects NSRF by uniformly increasing or decreasing the L_{Net} ($\approx 4\sigma\epsilon_{\text{snow}}T_{\text{snow}}^3\delta T_{\text{snow}}$) for all vegetation densities, while S_{Net} remains unchanged. This will lead to a uniform change in NSRF and hence no change in the optimal density (Figure 8c). We also note that an average snow albedo of 0.4 was used for the duration of analysis. Accounting for temporal variations in albedo over the entire

snow season resulting from variations due to snow aging and angular effects will influence the outgoing shortwave radiation and hence the variation of NSRF with $1/d$. Higher albedos reduce S_{Net} , leading to decrease in NSRF and the optimal density (Figure 8d). Similarly, S_{Net} is reduced by clumping (e.g., conifers; low G_s) and in species with relatively scattered canopy structure (low λ_s), leading to decrease in NSRF and the optimal density (the data are not shown). Despite these assumptions, this research clearly indicates that a net radiation minimum can occur in forests with intermediate densities and that physically based radiation transfer modeling based on discrete trees can be used to assess how the minimum point varies as a function of key variables that control snow cover energetics. Future work geared toward refining and accounting for snowmelt timing changes with $1/d$ will consider coupled changes in albedo, radiation, and snow cover dynamics.

3.2. Vegetation Density Influence on Net Radiation at the Forest Floor for Interspersed Clear and Cloudy Sky Conditions

[28] To consider effects of sky cloudiness on NSRF, the model was run using daily cloud cover data obtained from the closest National Renewable Energy Laboratory station to the studied site in Maine. Daily averaged τ_d and τ_b were also derived from NREL data set to estimate direct and diffuse shortwave components for cloudy sky conditions.

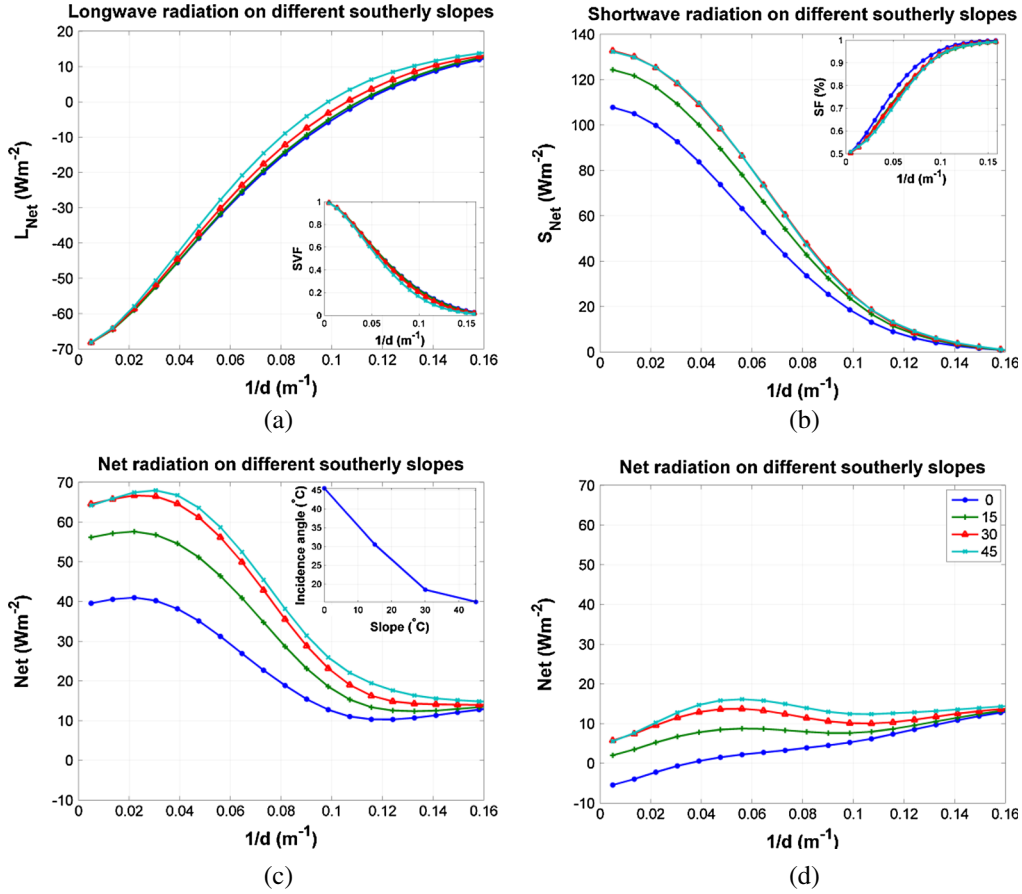


Figure 9. Effect of slope on the variability of radiation with vegetation densities on a south facing forest floor on different slopes: (a) net longwave radiation and sky view factor in clear sky conditions, (b) net shortwave radiation and shading fraction in clear sky conditions, (c) net radiation in clear sky conditions (inset figure shows average solar incidence angle at noon), and (d) net radiation when sky cloudiness is considered. All radiation values are averaged over the winter to summer solstices period.

Corrected sky emissivity was calculated using equation (36). Results suggest that compared to clear sky conditions, all incoming radiation components are affected by interspersed cloud cover. Cloud cover leads to higher sky emissivity resulting in an increase in $\downarrow L_{sky}$, while lower insolation may cause a decrease in canopy temperature contributing to a minor decrease in $\downarrow L_{crown}$ and $\downarrow L_{trunk}$ [Pomeroy *et al.*, 2009]. As a result, increase in L_{Net} in open areas was $\sim 15\%$ larger compared to clear sky conditions. Effect on L_{Net} is negligible in very dense forests ($1/d > 0.16 m^{-1}$) (Figures 7b and 7d). Shortwave radiation components are also influenced by cloud cover. Cloud cover reduces the direct shortwave component by increasing atmospheric extinction and enhances the diffuse shortwave component by increasing atmospheric scattering. As a result, global incoming shortwave radiation ($\downarrow S_{dir} + \downarrow S_{diff}$) decreases by $\sim 52\%$ compared to clear sky conditions (Figures 7b and 7d). Since the rate of decrease in shortwave radiation is markedly larger than rate of increase in longwave radiation, NSRF shows a monotonic increasing behavior with increasing vegetation density (Figure 7d). For locations with higher average of cloud cover than the studied site (the average cloud cover for Greenville, ME is about 56%), NSRF is expected to

expose a relatively rapid increase with vegetation density rather than the obtained results.

3.3. Effect of Slope on the Variation of Net Radiation in Relation to Tree Spacing

[29] To understand the impact of slope on variation in net radiation in relation to vegetation density, NSRF was calculated for a range of $1/d$ values on an inclined south facing hill-slope. Four different slope angles (0°, 15°, 30°, and 45°) were considered. Since forests are uncommon on very steep hillslopes, the maximum slope angle was limited to 45°. Changes in slope angle influences sky view factor, solar incidence angle (θ), shading fraction, and hence NSRF.

[30] For all slope angles considered in this experiment, SVF decreases with increasing vegetation density ($1/d$) as expected (Figure 9a). For lower forest densities where the distance between trees is large, the difference in sky view factor for different slope angles is very small. In relatively dense forests ($1/d > 0.06 m^{-1}$ or $cc > 10\%$), as slope increases, the angles subtended by the southern and northern trees increases and decreases, respectively. Since the rate of increase of the subtended angle by the southern trees are larger, sky view

Table 3. Minimum Radiation on Different North and South Facing Slopes

Slope Angle	Minimum $NSRF$ Occurs at $1/d \cong (\text{m}^{-1})$	Proportion of Radiation Relative to Open Area (%)	Proportion of Radiation Relative to Very Dense Forest (%)
0° (level forest)	0.12	26%	77%
15° south facing	0.13	22%	90%
30° south facing	0.16	22%	99%
45° south facing	0.17	22%	100%
15° north facing	0.09	41%	47%
30° north facing	0.05	100.0%	-92%
45° north facing	0.05	100.0%	-311%

factor decreases with increasing slope angle in denser forests. As noted in section 3.1, $\downarrow L_{\text{sky}}$ and $\downarrow L_{\text{tree}}$ are proportional to SVF and $1 - \text{SVF}$, respectively. On the other hand, $\uparrow L_{\text{snow}}$ is independent of SVF and hence to slope variations (equation (7)). Since $\varepsilon_{\text{crown}}$ and $\varepsilon_{\text{trunk}}$ are greater than ε_{sky} , under clear sky conditions, L_{Net} follows the trend of $\downarrow L_{\text{can}}$ and increases with decreasing SVF. As a result, SVF decreases with increase in slope, and L_{Net} increases slightly with increasing slope (Figure 9a). Solar incidence angle (θ) is also influenced by changes in slope. Seasonally averaged θ at noon shows

that θ decreases quickly with increase in slope from zero to 30° (Figure 9c, inset). Between slope angles of 30° and 45° (close to the site latitude), θ decreases at a lower rate. Shading fraction also varies with slope. Seasonally averaged shading fraction during daytime hours shows a decreasing trend for higher slopes (Figure 9b, inset). Furthermore, L_{path} is also smaller for higher slopes. Since solar incidence angle (θ) and shading fraction are largest for level forests, $\downarrow S_{\text{dir}}$ is smallest (equation (8)) for this slope case. Increasing slope therefore increases $\downarrow S_{\text{dir}}$ on the south facing hillslope. Since the radiation components are averaged from solstice to solstice, direct shortwave radiation is maximum for slope = 45°, at the modeling site. Furthermore, $\downarrow S_{\text{dif}}$ exhibits a decreasing trend with increase in slope (data not shown) because of decreasing SVF and $\cos(\beta/2)$ (see equation (15)). Since the comparative magnitude of $\downarrow S_{\text{dir}}$ is more than $\downarrow S_{\text{dif}}$, both $\uparrow S_{\text{snow}}$ and S_{Net} increase with slope (Figure 9b).

[31] As both S_{Net} and L_{Net} increase with slope, NSRF increases for all vegetation densities with increasing slope. In sparse forests ($1/d < 0.03 \text{ m}^{-1}$ or $cc < 3\%$), NSRF is highest relative to denser forests. On steeper slopes (hill slope angle $\geq 30^\circ$), the maximum NSRF occurs for $0.02 \text{ m}^{-1} < 1/d < 0.03 \text{ m}^{-1}$ ($1\% < cc < 3\%$) and is around 5% more than in open areas.

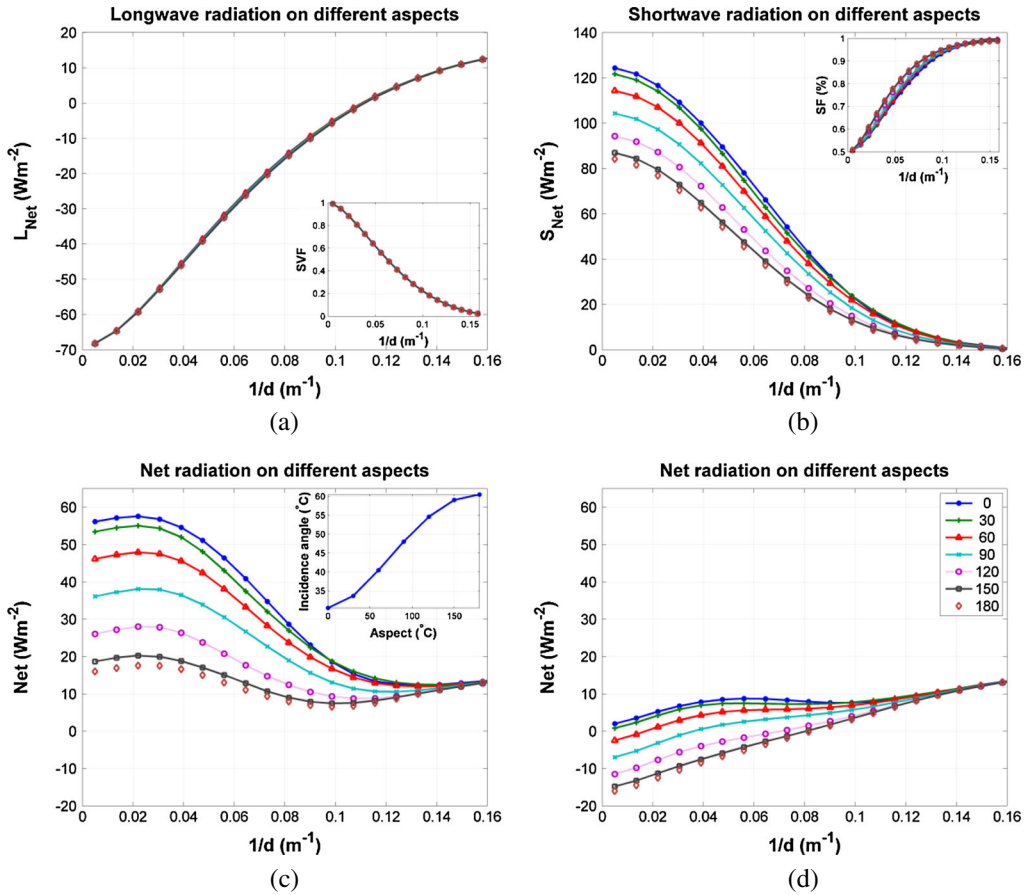


Figure 10. Effect of aspect on the variability of radiation with vegetation densities beneath forest canopies on a 15° slope: (a) net longwave radiation and sky view factor in clear sky conditions, (b) net shortwave radiation and shading fraction in clear sky conditions, (c) net radiation in clear sky conditions (inset figure shows solar incidence angle at noon), and (d) net radiation when sky cloudiness is considered. The 0° and 180° aspects respectively indicate south and north facing slopes. All radiation values are averaged over the winter to summer solstices period.

Table 4. Minimum Radiation for Different Aspects

Aspect Angle	Minimum NSRF Occurs at $1/d \approx (\text{m}^{-1})$	Proportion of Radiation Relative to Open Area (%)	Proportion of Radiation Relative to Very Dense Forest (%)
0° (south facing)	0.13	22%	90%
30°	0.14	23%	90%
60°	0.13	26%	87%
90°(east or west facing)	0.12	29%	77%
120°	0.10	33%	64%
150°	0.09	39%	54%
180° (north facing)	0.09	41%	47%

The ratio of net radiation at the vegetation density that minimizes S_{Net} relative to radiation at an unforested site increases with slope angle. In forests with hill slopes of 15°, net radiation on the forest floor at $1/d \approx 0.13 \text{ m}^{-1}$ or $cc \approx 47\%$ is about 78% less than the amount in open areas but only about 10% less than in dense forests ($1/d > 0.16 \text{ m}^{-1}$). For a slope angle equal to 30°, forests with $1/d > 0.16 \text{ m}^{-1}$ or $cc \approx 72\%$ are observed to have the minimum NSRF, and increasing vegetation density beyond this point has a negligible effect on NSRF, so this vegetation density effectively represents the point at which NSRF plateaus. The minimum NSRF is about 78% less than net radiation under open conditions. For an even higher slope angle of 45°, minimum radiation is obtained for very dense forests ($1/d > 0.16 \text{ m}^{-1}$) with magnitude of 78% less than NSRF in open areas. The vegetation density at which NSRF is minimized increases steadily from 0.12 m^{-1} to 0.16 m^{-1} with increasing slope (Table 3). This is due to a larger increase in S_{Net} than increase in L_{Net} with slopes for sparser tree densities. For very dense forests ($1/d > 0.16 \text{ m}^{-1}$), net shortwave radiation is mainly diffuse and is close to zero, and hence the changes in NSRF with slope in this setting are mostly governed by L_{Net} . L_{Net} in dense forests changes only marginally with different slopes. Hence, NSRF for different slopes are very similar for the highest canopy densities where $1/d > 0.16 \text{ m}^{-1}$ (Figure 9c). When sky cloudiness is considered, L_{Net} and S_{Net} show an increasing trend with increasing slope angle, similar to clear sky conditions. Additionally, changes in NSRF with aspect for very sparse forests ($1/d < 0.02 \text{ m}^{-1}$) are larger than changes in very dense forests ($1/d > 0.16 \text{ m}^{-1}$). Since increases in net shortwave radiation with slope are much larger than increases in longwave radiation, NSRF shows a nonmonotonic trend for higher slopes. For higher slopes, in very sparse and very dense forests, the rate of increase in L_{Net} is dominant to the rate decrease in S_{Net} , resulting in a local maximum in low-density and a local minimum in high-density forests. For slope angles of 30° and 45°, although the minimum radiation is still existent for sparse forests, a strong local minimum is exhibited at intermediate vegetation density ($1/d \approx 0.10 \text{ m}^{-1}$, Figure 9d).

3.4. Effect of Aspect on Radiation

[32] Variability of NSRF with vegetation density for different aspects was assessed using seven different orientations ranging from 0° to 180°, for a 15° forest slope. For this assessment, 0° indicates a south facing slope, while 180° represents a north facing slope. We note that a 15° slope angle was chosen as a typical mountainous site so that the influence

of aspect on variability of NSRF with vegetation density could be demonstrated.

[33] Aspect does not affect sky view factor; hence, for all aspects, longwave radiation components are the same as for south facing forests (Figure 10a). However, different aspects strongly affect solar incidence angle (θ), L_{path} , and hence shading fraction and transmissivity. Increasing both solar incidence angle and shading fraction reduces $\downarrow S_{\text{dir}}$ for increasing aspects (Figures 10b and 10c). The minimum $\downarrow S_{\text{dir}}$ is observed for the north facing hillslope as would be expected. Since both sky view factor and slope remain unchanged for different hillslope aspects, $\downarrow S_{\text{dif}}$ is independent of orientation angle. $\uparrow S_{\text{snow}}$ is proportional to $\downarrow S_{\text{dir}} + \downarrow S_{\text{dif}}$, and hence it decreases with increasing aspect. As a result, as aspect angle increases (from 0° to 180°), S_{Net} decreases and exhibits a minimum value for north facing forests as would be expected (Figure 10b).

[34] Monotonic increasing and decreasing trends of L_{Net} and S_{Net} with $1/d$ again leads to a minimum in NSRF for intermediate forest densities (Table 4). As noted in section 3.3, on a south facing hillslope (slope = 15°), NSRF is minimum for $1/d \approx 0.13 \text{ m}^{-1}$ or $cc \approx 47\%$. In this case, net NSRF is about 78% less than in open areas but only about 10% less than in dense forests ($1/d > 0.16 \text{ m}^{-1}$ or $cc > 75\%$). On hillslopes with an aspect angle, Z_s , of 30°, forests with $1/d \approx 0.13 \text{ m}^{-1}$ or $cc \approx 47\%$ have a minimum NSRF that is 77% less than net radiation in open areas and about 10% less than in the dense forests ($1/d > 0.16 \text{ m}^{-1}$) evaluated in this study. As aspect angle increases, the minimum NSRF occurs at lower vegetation densities. In other words, north facing forests have minimum NSRF for sparser tree densities than for south facing forests (Figure 10c). This is because more shortwave radiation is attenuated in sparse forests due to the relatively long path lengths on north facing slopes, whereas the longwave radiation emitted by the forest canopy is controlled by vegetation density and is not affected by aspect. Again, for very dense forests ($1/d > 0.16 \text{ m}^{-1}$), NSRF for different aspects are the same, similar to what has been previously observed [Ellis *et al.*, 2011]. When sky cloudiness is considered, similar to clear sky conditions, increasing aspects lead to decreases in S_{Net} . Since the decrease in S_{Net} is larger for sparser densities, the monotonic increasing trend of NSRF with vegetation density is sustained for all aspects (Figure 10d).

4. Summary and Conclusions

[35] A spatially distributed physically based model (FoRM) was run for a simulated white spruce forest stand near Greenville, ME, to develop a general understanding of how net snow cover radiation is sensitive to vegetation density, slope, and aspect in midlatitude coniferous forests. The results showed that in clear sky conditions minimum net radiation on the forest floor is observed for denser forests ($1/d > 0.12 \text{ m}^{-1}$ or $cc > 40\%$) with increasing slope to the south. When sky cloudiness was considered, minimum radiation occurs in open areas and very sparse forests. However, a local minimum is exhibited at an intermediate vegetation density ($1/d \approx 0.10 \text{ m}^{-1}$ or $cc \approx 28\%$) for high slope angles (30° and 45°). As the aspect of hillslopes change from south facing to north facing, in clear sky conditions, north facing forests have minimum net radiation

for sparser tree densities than that for south facing forests. When sky cloudiness is considered, net radiation increases almost linearly for north facing forests. Additionally, the variation of net radiation with vegetation density when cloudiness is considered is significantly less than that in clear sky conditions.

[36] The results suggest that appropriate forest management strategies that are aware of local climate factors, may be used to modulate radiation on the forest floor, and hence manage the melt rate of deposited snow. In managed white spruce level forests at $\sim 45^\circ\text{N}$ latitude with a vegetation density of about $1/d \approx 0.12 \text{ m}^{-1}$ equivalent to about 40% canopy closure, net radiation is less than 26% of the amount in open areas (for clear sky conditions) and about 77% of the amount in dense forests ($1/d > 0.16 \text{ m}^{-1}$ or $cc > 75\%$). Results also indicate that lower and higher densities are required to minimize net snow cover radiation on north and south facing slopes, respectively. These results should be used with caution when determining optimal densities to retain snow. Further sensitivity analyses should be performed to evaluate the effect of uncertainties in data and model structure, and in length of the snow season before management strategies are implemented for a specific location.

Appendix A: Calculation of Extraterrestrial Radiation and Solar Angles

[37] Extraterrestrial radiation for the N th day of the year is evaluated using [Kalogirou, 2009]

$$S_{\text{extr}} = S_c \left[1 + 0.033 \cos\left(\frac{360N}{365}\right) \right], \quad (38)$$

where $S_c = 1366.1 \text{ W/m}^2$ is solar constant. Solar incidence angle θ , the angle between the Sun's rays and the normal on a surface, is calculated for an inclined slope β with aspect Z_s using [Kalogirou, 2009]

$$\begin{aligned} \cos(\theta) = & \sin(L)\sin(\delta)\cos(\beta) - \cos(L)\sin(\delta)\sin(\beta)\cos(Z_s) \\ & + \cos(L)\cos(\delta)\cos(h)\cos(\beta) \\ & + \sin(L)\cos(\delta)\cos(h)\sin(\beta)\cos(Z_s) \\ & + \cos(\delta)\sin(h)\sin(\beta)\sin(Z_s), \end{aligned} \quad (39)$$

where δ is solar declination angle, h is solar hour angle, and L is latitudinal location. Solar declination angle (degree) for the N th day of the year is calculated by

$$\delta = 23.45 \sin\left(\frac{360}{365}(284 + N)\right). \quad (40)$$

[38] Solar hour angle is

$$h = 15(\text{AST}/60 - 12), \quad (41)$$

where AST is the apparent solar time (minute). Apparent solar time is estimated using

$$\text{AST} = \text{LST} + \text{ET} \pm 4(\text{SL} - \text{LL}) - \text{DS}, \quad (42)$$

where LST is local standard time (minute), ET is equation of time (minute), SL is standard longitude, LL is local

longitude, and DS is day light saving amount (minute). The value of the equation of time is obtained using

$$\text{ET} = 9.87 \sin(2B) - 7.53 \cos(B) - 1.5 \sin(B), \quad (43)$$

$$B = (N - 81) \frac{360}{364}. \quad (44)$$

[39] Solar zenith angle (ψ) for the latitude L is approximated by solving

$$\cos(\psi) = \sin(L)\sin(\delta) + \cos(L)\cos(\delta)\cos(h). \quad (45)$$

[40] Solar azimuth angle is evaluated by solving

$$\sin(z) = \frac{\cos(\delta)\sin(h)}{\sin(\psi)}. \quad (46)$$

[41] **Acknowledgments.** This study was supported by the Duke University start-up grant for new faculties, and by NSF-CBET Award 0854553. We also would like to thank Janet Hardy, Cold Regions Research and Engineering Laboratory, and Richard Essery, University of Edinburgh, for providing us the LSOS data.

References

- plantmaps.com (2012), PlantMaps-*Picea glauca*—White spruce interactive native range distribution map with USDA hardiness zones., <http://www.plantmaps.com/nrm/picea-glaucawhite-spruce-native-range-map.php>.
- Arbor Day Foundation (2012), ArborDayFoundation-Tree details—The tree guide <http://www.arborday.org/>.
- Aguado, E. (1985), Radiation balances of melting snow covers at an open site in the Central Sierra-Nevada, California, *Water Resour. Res.*, 21(11), 1,649–1,654, doi:10.1029/WR021i011p01649.
- Awanou, C. N. (1998), Clear sky emissivity as a function of the zenith direction, *Renew Energ.*, 13(2), 227–248.
- Berry, G. J., and R. L. Rothwell (1992), Snow ablation in small forest openings in southwest Alberta, *Can. J. Forest Res.*, 22(9), 1,326–1,331.
- Bohren, C. F., and D. B. Thorud (1973), Two theoretical models of radiation heat-transfer between forest trees and snowpacks, *Agric. For. Meteorol.*, 11(1), 3–16.
- Davis, R. E., J. P. Hardy, W. Ni, C. Woodcock, J. C. McKenzie, R. Jordan, and X. Li (1997), Variation of snow cover ablation in the boreal forest: A sensitivity study on the effects of conifer canopy, *J. Geophys. Res.*, 102(D24), 29,389–29,395.
- Dozier, J., and S. G. Warren (1982), Effect of viewing angle on the infrared brightness temperature of snow, *Water Resour. Res.*, 18(5), 1,424–1,434, doi:10.1029/WR018i005p01424.
- Dubayah, R., and P. M. Rich (1995), Topographic solar-radiation models for GIS, *Int J Geogr Inf Syst.*, 9(4), 405–419.
- Eck, T. F., and D. W. Deering (1990), Canopy albedo and transmittance in a boreal forest, *Remote Sensing Science for the Nineties*, 1-3, 883–886.
- Eck, T. F., and D. W. Deering (1992), Canopy albedo and transmittance in a spruce-hemlock forest in mid-September, *Agric. For. Meteorol.*, 59(3-4), 237–248.
- Elder, K., J. Dozier, and J. Michaelsen (1991), Snow accumulation and distribution in an alpine watershed, *Water Resour. Res.*, 27(7), 1,541–1,552, doi:10.1029/91WR00506.
- Ellis, C. R., J. W. Pomeroy, R. L. H. Essery, and T. E. Link (2011), Effects of needleleaf forest cover on radiation and snowmelt dynamics in the Canadian Rocky Mountains, *Can. J. Forest Res.*, 41(3), 608–620.
- Essery, R., J. Pomeroy, C. Ellis, and T. Link (2008a), Modelling longwave radiation to snow beneath forest canopies using hemispherical photography or linear regression, *Hydrol. Processes*, 22(15), 2,788–2,800.
- Essery, R., P. Bunting, J. Hardy, T. Link, D. Marks, R. Melloh, J. Pomeroy, A. Rowlands, and N. Rutter (2008b), Radiative transfer modeling of a coniferous canopy characterized by airborne remote sensing, *J. Hydrometeorol.*, 9(2), 228–241.
- Flerchinger, G. N., W. Xaio, D. Marks, T. J. Sauer, and Q. Yu (2009), Comparison of algorithms for incoming atmospheric long-wave radiation, *Water Resour. Res.*, 45, W03423, doi:10.1029/2008WR007394.

- Gary, H. L. (1974), Snow accumulation and snowmelt as influenced by a small clearing in a lodgepole pine forest, *Water Resour. Res.*, 10(2), 348–353, doi:10.1029/WR010i002p00348.
- Gay, L. W. (1968), Radiation balance of a forest canopy, *Bull. Am. Meteorol. Soc.*, 49(1), 187–196.
- Gay, L. W., K. R. Knoerr, and M. O. Braaten (1971), Solar radiation variability on floor of a pine plantation, *Agric. For. Meteorol.*, 8(1), 39–50.
- Gelfan, A. N., J. W. Pomeroy, and L. S. Kuchment (2004), Modeling forest cover influences on snow accumulation, sublimation, and melt, *J. Hydrometeorol.*, 5(5), 785–803.
- Gilman, E. F., and D. G. Watson (1994), *Picea glauca* white spruce, in *Department of Agriculture*.
- Golding, D. L., and R. H. Swanson (1978), Snow accumulation and melt in small forest openings in Alberta, *Can. J. Forest Res.*, 8(4), 380–388.
- Gryning, S. E., E. Batchvarova, and H. A. R. De Bruin (2001), Energy balance of a sparse coniferous high-latitude forest under winter conditions, *Bound.-Lay. Meteorol.*, 99(3), 465–488.
- Gustafson, J. R., P. D. Brooks, N. P. Molotch, and W. C. Veatch (2010), Estimating snow sublimation using natural chemical and isotopic tracers across a gradient of solar radiation, *Water Resour. Res.*, 46, W12511, doi:10.1029/2009WR009060.
- Hardy, J. P., R. E. Davis, R. Jordan, X. Li, C. Woodcock, W. Ni, and J. C. McKenzie (1997), Snow ablation modeling at the stand scale in a boreal jack pine forest, *J. Geophys. Res.*, 102(D24), 29,397–29,405.
- Hardy, J. P., R. Melloh, G. Koenig, D. Marks, A. Winstal, J. W. Pomeroy, and T. Link (2004), Solar radiation transmission through conifer canopies, *Agric. For. Meteorol.*, 126(3-4), 257–270.
- Hendrick, R. L., B. D. Filgate, and W. M. Adams (1971), Application of environmental analysis to watershed snowmelt, *J. Appl. Meteorol.*, 10(3), 418–429.
- Hottel, H. C. (1976), Simple model for estimating transmittance of direct solar-radiation through clear atmospheres, *Sol. Energy*, 18(2), 129–134.
- Hutchison, B. A., and D. R. Matt (1977), The distribution of solar radiation within a deciduous forest, *Ecological Monographs*, 47(2), 185–207.
- Jost, G., M. Weiler, D. R. Gluns, and Y. Alila (2007), The influence of forest and topography on snow accumulation and melt at the watershed-scale, *J. Hydrol.*, 347(1-2), 101–115.
- Kalogirou, S. (2009), *Solar Energy Engineering: Processes and Systems*, xv, Elsevier/Academic Press, Burlington, MA, pp. 760.
- Kaminsky, K. Z., and R. Dubayah (1997), Estimation of surface net radiation in the boreal forest and northern prairie from shortwave flux measurements, *J. Geophys. Res.*, 102(D24), 29,707–29,716.
- Kaufmann, M. R., C. B. Edminster, C. A. Troendle, and Rocky Mountain Forest and Range Experiment Station (Fort Collins Colo.) (1982), *Leaf Area Determinations for Subalpine Tree Species in the Central Rocky Mountains*, 7p., Rocky Mountain Forest and Range Experiment Station, Forest Service, U.S. Dept. of Agriculture, Fort Collins, Colo.
- Kreith, F., and J. F. Kreider (2011), *Principles of Sustainable Energy*, xxiii, 855 p., 816 p. of plates pp., CRC Press, Boca Raton, FL.
- Kumar, L., A. K. Skidmore, and E. Knowles (1997), Modelling topographic variation in solar radiation in a GIS environment, *Int J Geogr Inf Sci*, 11(5), 475–497.
- Lawler, R. R., and T. E. Link (2011), Quantification of incoming all-wave radiation in discontinuous forest canopies with application to snowmelt prediction, *Hydrol. Processes*, 25(21), 3,322–3,331.
- Link, T. E., and D. Marks (1999), Point simulation of seasonal snow cover dynamics beneath boreal forest canopies, *J. Geophys. Res.*, 104(D22), 27,841–27,857.
- Lundquist, J. D., and A. L. Flint (2006), Onset of snowmelt and streamflow in 2004 in the western United States: How shading may affect spring streamflow timing in a warmer world, *J. Hydrometeorol.*, 7(6), 1,199–1,217.
- Male, D. H., and R. J. Granger (1981), Snow surface-energy exchange, *Water Resour. Res.*, 17(3), 609–627, doi:10.1029/WR017i003p0060.
- Marks, D., and J. Dozier (1979), Clear-sky longwave radiation model for remote alpine areas, *Arch Meteor Geophys B*, 27(2-3), 159–187.
- Mathews, T. R., Y. Malhi, and H. Iwata (2012), Calculating downward longwave radiation under clear and cloudy conditions over a tropical lowland forest site: An evaluation of model schemes for hourly data, *Theor. Appl. Climatol.*, 107(3-4), 461–477.
- Matzarakis, A., and O. Matuschek (2011), Sky view factor as a parameter in applied climatology—Rapid estimation by the SkyHelios model, *Meteorol. Z.*, 20(1), 39–45.
- Melloh, R. A., J. P. Hardy, R. N. Bailey, and T. J. Hall (2002), An efficient snow albedo model for the open and sub-canopy, *Hydrol. Processes*, 16(18), 3,571–3,584.
- MFC (1908), *Forest trees of Maine*, p. v., Augusta.
- Monteith, J. L., and M. H. Unsworth (2008), *Principles of Environmental Physics*, 3rd ed., xxi, 418 p., Elsevier, Amsterdam; Boston.
- Musselman, K. N., N. P. Molotch, and P. D. Brooks (2008), Effects of vegetation on snow accumulation and ablation in a mid-latitude sub-alpine forest, *Hydrol. Processes*, 22(15), 2,767–2,776.
- NCDC (2012), <http://www.ncdc.noaa.gov/oa/ncdc.html>, Accessed July, 2012.
- Nilson, T. (1971), A theoretical analysis of the frequency of gaps in plant stands, *Agric. For. Meteorol.*, 8(0), 25–38.
- NREL (2012), National Renewable Energy Laboratory, www.nrel.gov. Accessed February 2013.
- NSIDC (2013), The Cold Land Processes Field Experiment, http://nsidc.org/data/clpx/clpx_data.html.
- Pluss, C., and A. Ohmura (1997), Longwave radiation on snow-covered mountainous surfaces, *J. Appl. Meteorol.*, 36(6), 818–824.
- Pomeroy, J. W., and K. Dion (1996), Winter radiation extinction and reflection in a boreal pine canopy: Measurements and modelling, *Hydrol. Processes*, 10(12), 1,591–1,608.
- Pomeroy, J. W., D. Marks, T. Link, C. Ellis, J. Hardy, A. Rowlands, and R. Granger (2009), The impact of coniferous forest temperature on incoming longwave radiation to melting snow, *Hydrol. Processes*, 23(17), 2,513–2,525.
- Prata, A. J. (1996), A new long-wave formula for estimating downward clear-sky radiation at the surface, *Q. J. R. Meteorol. Soc.*, 122(533), 1,127–1,151.
- Price, A. G., and T. Dunne (1976), Energy-balance computations of snowmelt in a subarctic area, *Water Resour. Res.*, 12(4), 686–694, doi:10.1029/WR012i004p00686.
- Rango, A., and V. F. Vankatwijk (1990), Climate change effects on the snowmelt hydrology of western North-American mountain basins, *IEEE T Geosci Remote*, 28(5), 970–974.
- Rasmus, S., R. Lundell, and T. Saarinen (2011), Interactions between snow, canopy, and vegetation in a boreal coniferous forest, *Plant Ecol. Divers.*, 4(1), 55–65.
- Reifsnnyder, W. E., and H. W. Lull (1965), *Radiant Energy in Relation to Forests*, vi, 111 p., U.S. Dept. of Agriculture, Forest Service; For sale by the Superintendent of Documents, U.S. Govt. Print. Off., Washington.
- Sicart, J. E., J. W. Pomeroy, R. L. H. Essery, J. Hardy, T. Link, and D. Marks (2004), A sensitivity study of daytime net radiation during snowmelt to forest canopy and atmospheric conditions, *J. Hydrometeorol.*, 5(5), 774–784.
- Sicart, J. E., J. W. Pomeroy, R. L. H. Essery, and D. Bewley (2006), Incoming longwave radiation to melting snow: Observations, sensitivity and estimation in northern environments, *Hydrol. Processes*, 20(17), 3,697–3,708.
- Stewart, I. T., D. R. Cayan, and M. D. Dettinger (2005), Changes toward earlier streamflow timing across western North America, *J. Climate*, 18(8), 1,136–1,155.
- Todhunter, P. E., F. Xu, and J. M. Buttle (1992), A model of net-radiation over suburban snowpacks, *Atmos. Environ. Part B*, 26(1), 17–27.
- USACE (1956), *Snow Hydrology; Summary Report of the Snow Investigations*, xxv, 437 p. pp., North Pacific Division, Corps of Engineers, U.S. Army, Portland, Or.,.
- Varhola, A., N. C. Coops, M. Weiler, and R. D. Moore (2010), Forest canopy effects on snow accumulation and ablation: An integrative review of empirical results, *J. Hydrol.*, 392(3-4), 219–233.
- Wang, Z., and X. B. Zeng (2010), Evaluation of snow albedo in land models for weather and climate studies, *J. Appl. Meteorol. Clim.*, 49(3), 363–380.
- Warren, S. G. (1982), Optical-properties of snow, *Rev. Geophys.*, 20(1), 67–89.
- Warren, S. G., and W. J. Wiscombe (1980), A model for the spectral albedo of snow. 2. Snow containing atmospheric aerosols, *J. Atmos. Sci.*, 37(12), 2,734–2,745.
- Winkler, R., and J. Roach (2005), Snow accumulation in BC's southern interior forests, *Streamline Watershed Management Bulletin*, 9(1).
- Wiscombe, W. J., and S. G. Warren (1980), A model for the spectral albedo of snow. 1. Pure snow, *J. Atmos. Sci.*, 37(12), 2,712–2,733.
- Wong, L. T., and W. K. Chow (2001), Solar radiation model, *Appl. Energy*, 69(3), 191–224.